Characterization, Processing and Performance of Belle Fourche Shale for Ceramics

Samuel Kessinger, South Dakota School of Mines and Technology, Rapid City, SD

Kiran Green, South Dakota School of Mines and Technology, Rapid City, SD

Jacob Petersen, South Dakota School of Mines and Technology, Rapid City, SD

Jon J. Kellar, South Dakota School of Mines and Technology, Rapid City, SD

Keywords: shale processing, shale characterization, ceramics

Abstract

Belle Fourche Shale was processed and characterized for use as a clay-based ceramic. The shale was wet sieved to produce particles that were +/- 150 μm. X-ray diffraction (XRD) revealed that the -150 μm material was enriched in clay content compared to the unprocessed materials, whereas the oversize material was enriched in quartz compared to the undersize sample. Particle size analysis was performed on the - 150 μm sample, which showed that the median particle size was around 10 μm. Scanning electron microscopic (SEM) analysis further confirmed the small plate size, which appeared to be primarily layered clay particles. Next, the -150 μm particles were rolled into a green body, dried at room temperature, and fired at 998 ºC. The fired piece was analyzed by XRD and contained 6 wt% hematite, 55% quartz, 19% microcline, and various other minor amounts of minerals. When fired at 1152 ºC, mullite was found with increasing hematite compared to the 998 ºC firing. A multi-spectral analyzer was used to quantify the color change of the 998 ºC fired (orange) to the 1152 ºC fired (red) samples. Micro-computed tomography (Micro-CT) of the unfired body exhibited very few large pores, while the piece fired at 998 ºC also

exhibited few and small pores, the overall porosity of the fired body increased. Microhardness data, obtained from the aforementioned samples, resulted in Vickers Hardness (HV1.0) values of 70.8 HV1.0 (998 ℃) and 485.7 HV1.0 (1152 ℃). Three-point bend testing was performed, giving an average strength of 23 MPa on pieces fired at 998 ℃. The average bending strength of the samples fired at 1152 ℃, was 55 MPa.

Introduction

Shale is composed of compressed clay and other earth abundant minerals containing SiO_2 and Al_2O_3 [1]. Belle Fourche Shale (BFS) is a large shale deposit within portions of North and South Dakota, Montana, and Wyoming. The BFS deposit was formed in the late Cretaceous period and formed at the bottom of the Western Interior Seaway [2-6]. During the late Cretaceous period the seaway spanned the middle of the present day North American continent that was undergoing heavy volcanic activity. The volcanic activity deposited the mineral content in the BFS.

BFS is considered by the US Geological Survey as a bentonitic shale [7]. The only known commercial use of BFS is as a feedstock component for cement production. The classification of BFS as a bentonitic shale implies that the ore contains significant amounts of the smectite clay (tetrahedral sheets of silica sandwiching a central octahedral sheet of alumina) montmorillonite ($(Na,Ca)_{0.33}(Al,Mg)_2(Si_4O_{10})(OH)_2 \cdot nH_2O$) [2].

Shale-based ceramics (shale which has been processed, shaped into a green body, and fired) have been the subject of recent research for use in a variety of applications including use as thermal storage materials [8-12]. Thermal storage ceramics offer an inexpensive means to capture heat from thermal (e.g., nuclear, solar and wind) power plants [13,14]. The interest in shale-based ceramics is because they can possess relatively high thermal storage capacity, good thermal shock

resistance, and are relatively inexpensive to process. This research was conducted to determine the efficacy of BFS as a feedstock for clay-based ceramic materials.

Materials and Methods

Sample Collection, Wet Sieving, Drying and Firing

Raw BFS was collected from the edge of the South Dakota School of Mines and Technology campus (44°0411"N 103°12'11"W). [15] Figure 1 shows a macroscopic image of the raw BFS sample. The size distribution of the collected material is represented by the Gaudin-Schuhmann (sieve analysis) plot shown in Figure 2. The Gaudin-Schuhmann analysis showed the raw shale to have a distribution modulus of 0.19 and a size modulus of 18.7 mm. The raw shale (see Figure 1) has a distinctly layered macroscopic structure with many large sheets, as specified by the size modulus. To begin the processing the BFS was placed in water for two days to help swell and equilibrate the clay with moisture content. After the two days, the BFS was noticeably softer and easily exfoliated into smaller particles. The slurry was manually pushed through a 100 mesh screen (openings ~150 μm) with copious amounts of tap water. At this stage of processing the BFS was very hydroplastic and the wet sieving noticeably exfoliated the shale. The wet sieving left significant water with the -150 μm BFS portion, and consequently, the slurry was allowed to settle for a day. A small fraction of BFS (approximately 10 wt%) did not easily push through the screen, and this oversize sample fraction was dried for later analysis. With regard to the -150 μm sample, the excess water was decanted, and the particles were left to dehydrate in ambient air for three days. Next, the oversized and undersized particles from the wet sieving process were placed in a drying oven at 60 °C overnight. Finally, the powders were broken into particles using a mortar and pestle. Each sample was placed in a clean, dry bottle.

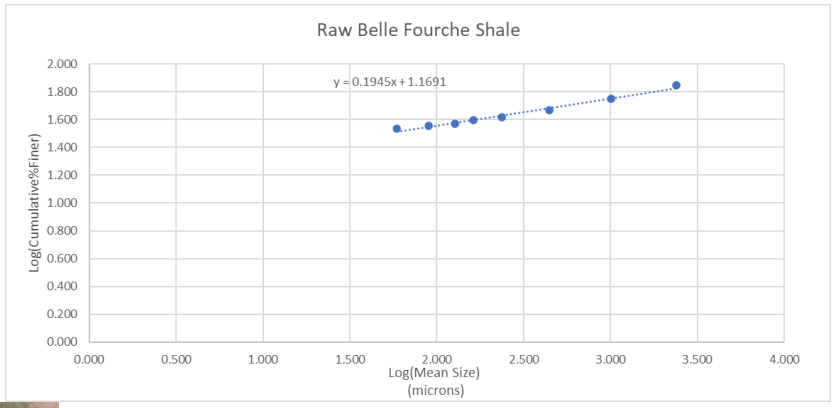

The dry -150 μm sample particles were then rehydrated by working the BFS by hand until there was an approximate solid-to-liquid ratio of 3:1. This green body was used for subsequent processing.

Figure 1. Image of raw BFS.

Figure 2. Gaudin-Schuhmann plot from raw BFS.

Sample Fabrication, Firing and Three-Point Bend Testing

The green body described in the previous section was used to form three-point bend test specimen. The mold shown in Figure 3 for three-point bend testing was 3-D printed (plastic) to create openings with dimensions 55 mm x 6 mm x 5 mm.

Figure 3. 3-D printed molds used to create three-point bend coupons.

The green body material was rolled (conventional rolling pin) into the mold. The mold dimensions were chosen to conform to ASTM Standard C1161-13. [16] The green body made from BFS exhibits nearly 15% shrinkage upon drying under ambient conditions. Thus the mold was fabricated larger than the desired size for three-point bend testing (45 mm x 4 mm x 3 mm). The shrinkage during air drying caused the samples to pull from the mold, and the samples were allowed to dry under ambient conditions for a day. After air drying the samples still contain some bound water associated with the clay and mica that fully evaporates once the samples are fired at elevated temperature.

The samples were fired in an electric kiln (Skutt, Model: KMT-1027-3) at a programmed Cone 06 bisque fire. Cone 06 firing began by climbing 100 ℃ per hour until 200 ℃ was reached. The temperature was held at 200 ℃ for two hours to expel remaining water. The temperature was increased by 150 ℃ per hour until the kiln reached 500 ℃. Finally, the kiln increased in temperature 325 ℃ every hour until it reached final temperature 998 ℃. The kiln was held at this temperature for 30 minutes and allowed to cool to room temperature. Firing of samples at a higher

temperature (Cone 3) also occurred. The same firing schedule described above occurred, with the exception of a higher final firing temperature of 1152 ℃.

To ensure the desired three-point dimensions were attained, fired sample coupons were ground to the desired length, width, and thickness on a grinding table using 240 grit paper. The samples were measured, and the centers were marked. The samples were placed on a three-point bend test apparatus (MTS 858) on a Test Resources three-point bend fixture with a pin diameter of 4 mm. The gap between the pins was set at 20 mm and ASTM Standard C1161-13 procedures were followed to determine sample bend strength.

X-ray Diffraction (XRD)

The oversized and undersized particles from the wet sieving process were dried for XRD analysis. Similarly, samples from the fired samples were ground into a powder for XRD analysis. A Malvern PANalytical Empyrean X-ray diffraction instrument equipped with a cobalt source was used for analysis of these samples.

Optical Microscopy

A Leica optical microscope was used to capture images of dried undersized and oversized material after sieving. Samples were placed on a white sheet of paper to give clarity to the images. Magnification and focus were changed as needed to produce the images taken with the microscope.

Fine Particle Size Analysis

Particle size distribution was performed on the fine, undersized material from wet sieving. The sample containment unit in the instrument (Microtrac) was filled with distilled water, rinsed, and flushed twice before measurement began. For analysis, undersized particles were added to the

sample in slurry form directly after wet sieving. Ten measurements were taken for 30 seconds each.

Scanning Electron Microscopy

A Thermo Fisher Scientific Helios 5CX scanning electron microscope was used to analyze the undersize particles. This analysis included the clay-like plates, determination of the plate sizes, and other undersized particles. Some samples were prepared by mounting dried samples onto carbon tape. The samples were secured with carbon paint to facilitate conductivity. Other samples were prepared by diluting (with water) powder that had been ground in a mortar. Once diluted, a drop was added to flat carbon tape and dried overnight in a low-temperature oven.

X-ray Fluorescence (XRF) Spectroscopy

Crushed and powdered samples of the oversized, undersized, and raw material of the BFS were analyzed through use of an Olympus Vanta X-Ray Fluorescence (XRF) portable spectrometer. The powders were placed in plastic canisters with a thin mylar film over the bottom. The XRF spectrum was run, and the elements' signals were recorded and reported in terms of relative metal oxides present. Oxides via XRF were that of magnesium (MgO), aluminum (Al_2O_3), silicon (SiO_2), potassium (K_2O), calcium (CaO), titanium (TiO_2), and iron (Fe_2O_3) were recorded.

Micro-computed Tomography

Micro-computed tomography (Micro-CT) analysis was performed using an Xradia Micro-CT. Both a rolled and fired (998 °C) sample and a rolled and unfired sample were analyzed for porosity and pore size. Micro-CT data was analyzed using Avizo-3D software. The stacked images were normalized for exposure variations, then a median filter was applied. The stacked images

were segmented, to isolate the voids from the surrounding solid material. Finally, a volume fraction, over the entire 3D body, was calculated. This processing step was applied to both the unfired sample, as well as the fired sample. Cross-sectional images of the samples were captured and overlayed with a mask to expose the voids present.

Microhardness

Vickers Hardness (HV1.0) was measured using a Buehler Micro-hardness tester. The machine utilizes a diamond, right pyramid-shaped, indenter. The indenter has a square base with a peak angle of 136 degrees. A 1 kilogram-force (kgf) load was applied to the sample for 15 seconds. The two diameters (from peak to peak) of the resulting indentation were then measured.

Both fired samples were indented 15 times, to negate the influence individual phases might have on the bulk hardness. The indentations were measured using an optical microscope and confirmed using a scanning electron microscope (ThermoScientific Axia SEM). The resulting indentation measurements were used to calculate the average Vickers Hardness (HV1.0) of each sample. The same technique could not be applied to the unfired ceramic, given its relative softness compared to the fired ceramic.

Results and Discussion

Optical Microscopy

Figure 4 is an image captured with an optical microscope of the undersize material after drying. Note the very fine mineral grains and a wide range of colored particles, reflective of the with variety of minerals found by XRD analysis (see Table 1). The particles are much smaller than 150 μm, which is to be expected from the wet sieving process. The pieces of oversized (+150 μm)

shale after drying shown in Figure 5 are all nearly 2 mm across in at least one direction. Even in the dry condition the oversized sample was not friable compared to the raw BFS.

Fine Particle Size Analysis

Figure 6 shows the particle size distribution of the undersized BFS that was analyzed in a slurry as described earlier. All particles present in the slurry were less than 30 μm, with the median particle size (50% passing) at just under 10 μm. This is much smaller than the 150 μm size restricted by the screen in the sieving process, and is in agreement with the fine particles imaged by optical microscopy (see Figure 4).

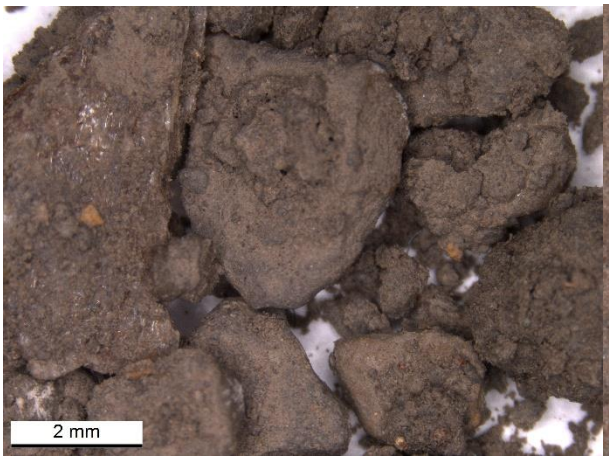

Figure 4. Optical image of undersized BFS.

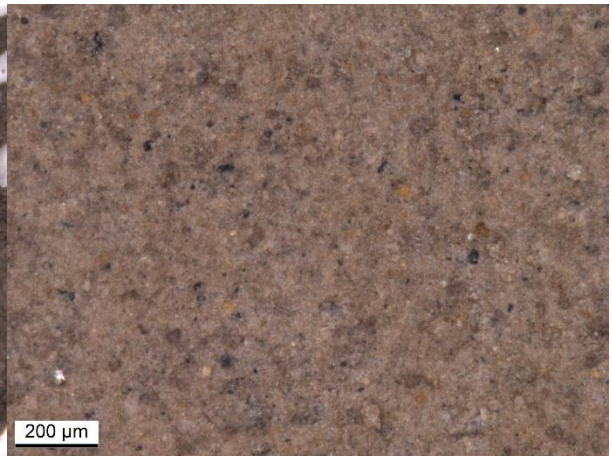

Figure 5. Optical image of oversized BFS.

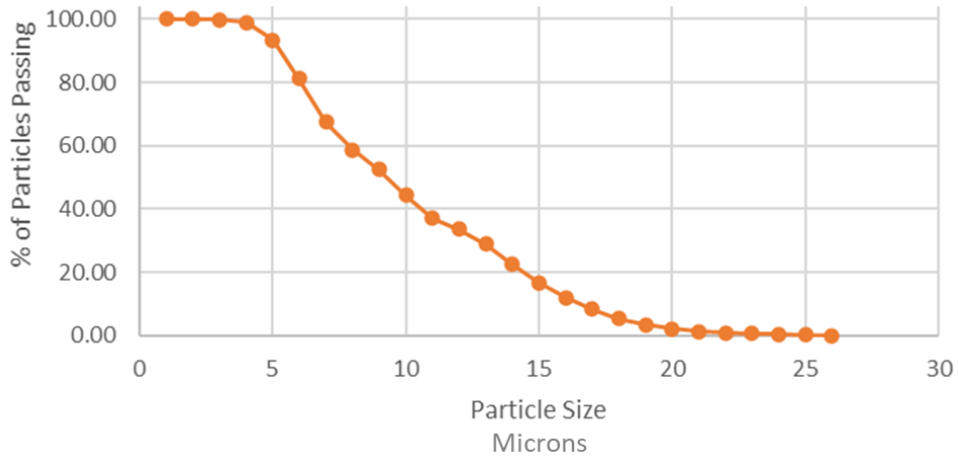

Figure 6. Particle size distribution of undersize BFS sample showing % of particles over size versus particle size (microns).

Scanning Electron Microscopy (SEM)

SEM was used to image the particles of the undersized sample. A carbon coating was applied to reduce charging of the sample, as BFS is not conductive. A representative image of the undersize material (see Figure 7) shows a significant number of high-aspect ratio platey particles, a characteristic morphology of clay minerals. The particles are less than 500 nm in diameter with a thickness of several nm. The plates are arranged randomly, likely an artifact from the drying process.

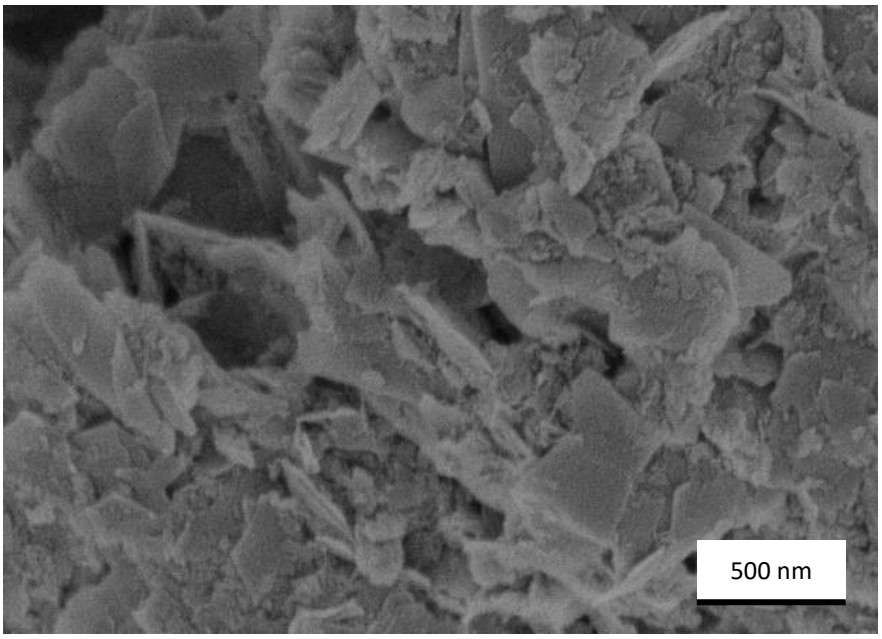

Figure 7. SEM image of BFS undersize sample.

X-ray Fluorescence (XRF) Spectroscopy

Table 2 shows the XRF results for the raw, undersize and oversized samples in terms of a mixed-oxide analysis. The XRF results are important in terms of interpreting whether the BFS has the necessary oxide 'building blocks' to form a strong ceramic material after firing. In this regard, the BFS XRF analysis shows that there is significant SiO_2, Al_2O_3 and Fe_2O_3 content in all three samples analyzed. The BFS can be compared to other shale samples that have been considered for use as ceramics. For example, Deng and Li [8] reported a similar mixed oxide analysis for an eastern Chinese shale deposit, although BFS has roughly half the Al_2O_3 and Fe_2O_3 content in comparison. Hajjaji and Khalfaouri [10] reported a similar mixed oxide analysis for a Moroccan shale, but once again, BFS, in comparison, has lower Al_2O_3 and Fe_2O_3 content.

Table 1. Mixed metal oxide XRF analysis for BFS samples.*

	% MgO	% Al_2O_3	% SiO_2	% K_2O	% CaO	% TiO_2	% Fe_2O_3

Oversized	0.8	13.9	54.2	2.6	0.4	0.7	3.9
Undersized	-	14.9	56.5	2.8	0.2	0.7	4.3

**balance not reported above are light elements, not explicitly reported by XRF*

X-ray Diffraction (XRD)

Figure 8 shows an example XRD spectrum for the dry, raw BFS. Table 1 shows the phase normalized XRD results after processing. Quartz, smectite clays (e.g., montmorillonite), kaolinite, and muscovite comprise the majority of minerals in the BFS sieved material. In the oversize sieve material (+150 μm) quartz is the predominant (55.7%) mineral present. The sieved undersized (-150 μm) contains a preponderance of smectite clays, with diminishing quartz compared to the oversized sample. Smectite clays are the greatest percentage (35.5%) of the sample, followed by quartz, muscovite, and kaolinite. The presence of clays helps confirm the interpretation of the SEM image shown in Figure 7.

When the material was fired at 998 ºC quartz represented more than half of the composition. The increase in quartz after firing can be attributed to the decomposition of muscovite and clay. Furthermore, the firing resulted in the presence of microcline and hematite. The sample fired at 1152 ºC showed no microcline and the creation of mullite and an amorphous glass phase compared to the 998 ºC fired sample.

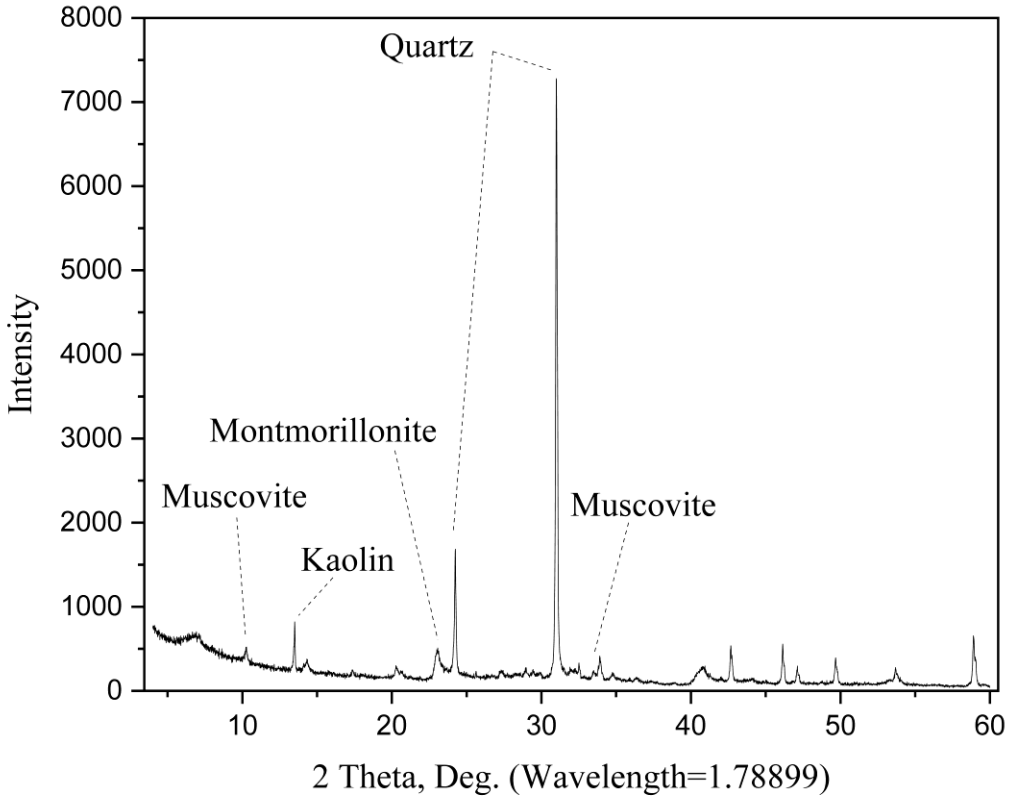

Figure 8. XRD Spectrum for raw BFS sample.

Table 2. Relative amount of minerals in BFS determined by XRD.

	Quartz	Smectites	Kaolinite	Muscovite	Microcline	Hematite	Mullite	amorphous
Oversized	55.7	3.6	6.1	34.6	-	-	-	-
Undersized	32.1	35.5	6.9	25.5	-	-	-	-
Fired (998 °C)	54.4	10.2	-	-	18.9	6.3	-	-
Fired (1152 °C)	46.0	-	-	-	-	10.5	13.7	24.6

One can conclude that the sieving process was effective at exfoliating the clays, causing them to occur in the undersize sample preferentially compared to the quartz. This segregation

allows for formation of a green body clay with good plasticity. The XRD results from the fired samples will be interpreted with the three-point bend testing section that follows.

Three-Point Bend Testing

Ten fired (998 °C) samples and five samples fired at 1152 °C, made to ASTM standard 1161 B [16], were analyzed using Equation 1.

$$S = 3PL/2bd^2 \qquad \text{Equation 1}$$

where:

P = break force [N],
L = outer (support) span [mm],
b = specimen width [mm], and
d = specimen thickness [mm]

The three-point bend strength for the 998 °C fired samples was 23 MPa. The three-point bend strength for the 1152 °C fired samples was 55 MPa. The increase in strength with increased firing temperature can be interpreted in terms of the XRD results shown in Table 2, specifically the increase in hematite content, and the formation of mullite and an amorphous phase at the higher firing temperature. Mullite is a non-stoichiometric compound comprised of Al_2O_3 and SiO_2 building blocks (e.g., $3Al_2O_3{\cdot}2SiO_2$), known for its high strength and high thermal stability. Mullite has been reported to be a decomposition product from muscovite ($KAl_2(AlSi_3O_{10})(F,OH)_2$) [17] which was present at relatively high amounts in the undersize sample (see Table 2).

The increase in hematite with firing temperature aids in the formation of a glassy amorphous phase, which should also aid in overall strength. Iron oxides, such as hematite, act as a flux [1] and promote the formation of the amorphous glass phase. The increase in hematite with firing temperature can also be seen visually through the visible color change from an orange (998 °C firing) to red (1152 °C firing) as shown in Figure 8. The specimen shown in Figure 9 were also

analyzed by a Foster and Freeman Video Spectral Comparator (VSC8000/HS) and the Commission Internationale de l'Elcairage (CIE) color space coordinates determined. [18] The CIE coordinates shown in Figure 9 confirmed the orange to red shift with higher firing temperature.

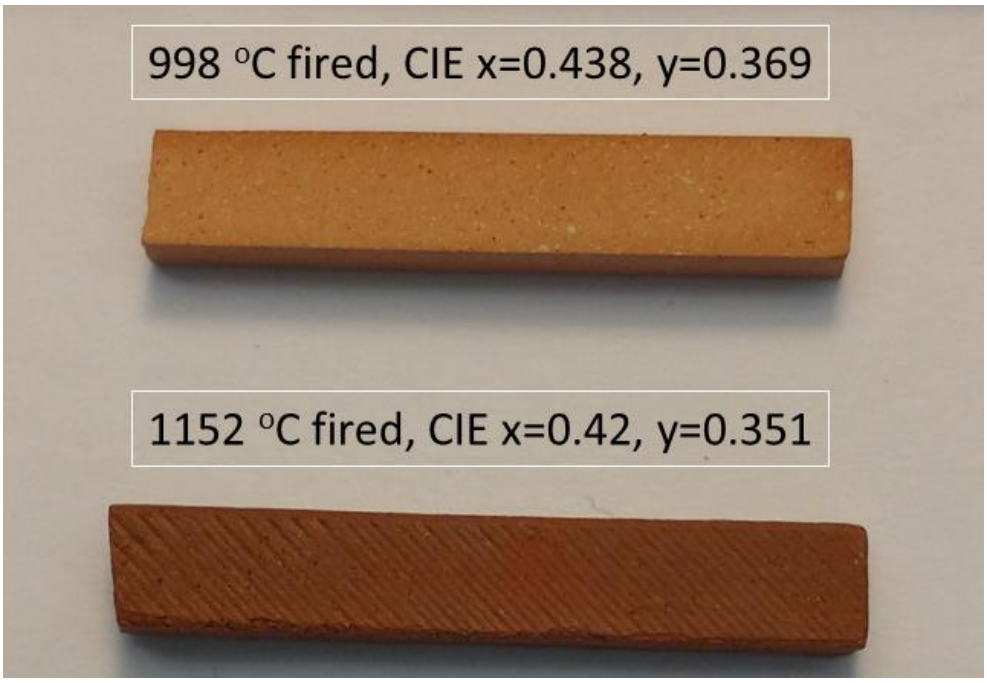

Figure 9. Three-point bend specimen, top fired at 998 °C and bottom fired at 1152 °C, with CIE color coordinates noted.

The three-point bend strength of 55 MPa can be compared to the strength found by Deng and Li [8] for an amended eastern Chinese shale. Deng and Li found a maximum three-point bend strength of 125.76 MPa. However, that three-point bend strength was found with a base shale sample (with differing metal oxide content, as noted earlier) that was amended with additional minerals (75% shale, 10% kaolin, 10% potash feldspar and 5% soda feldspar) and analyzed over seven firing temperatures to maximize the strength. We believe that with similar amendments and optimal firing that that similar strengths could be achieved for the fired BFS.

Micro-CT

The micro-CT images in Figures 10 (A/B) showed that pores were found within the sample, both before (Figure 9.A) and after firing (Figure 9.B) at 998 ºC. Following the firing, the porosity of the sample increases, as compared to the unfired sample. The reason for the increase in porosity may be attributed to the chemistry changes with firing as noted earlier (see Table 2). Many of the pores (shown in black), are smaller than 100 μm, with many close to 10 μm in size. Less porosity in a fired ceramic helps ensure greater strength and durability. The pores in the unfired sample do not indicate random distribution, with many oriented longitudinally, along the sample's long axis, indicating texturing imposed on the clay particles from processing. In contrast, the majority of the porosity observed within the fired sample, are distributed randomly throughout the sample, exhibiting lower longitudinal texturing. The brighter, white spots, in Figure 9A are areas of high density (e.g., hematite, or a similar dense mineral phase). The determination of the identity of the dense phases requires future investigation.

The resulting void fraction of the samples are as follows; fired (998 ºC), body void fraction: 0.029 (or 2.9%), unfired body void fraction: 0.009 (or 0.9%). The Micro-CT analysis conducted on the samples, as described above, was conducted at an approximate resolution of 3.5 μm per pixel. This, in turn, diminishes the ability of this analysis to conclusively observe the smallest voids present in these samples. Therefore, the reported porosities of these samples only include voids significantly larger than 3.5 μm^3. Further analysis, at a finer resolution, would provide definitive porosity (void volume fraction) data.

Microhardness

Vickers hardness (HV1.0) is calculated using Equation 2. A load of 1 kgf was used when indenting the samples; therefore, the equation has been amended to include only one variable, d,

or average diameter. Due to the small scale of the indentations, units of μm were used. These units must first be converted to mm prior to being used in Equation 2.

$$\text{HV1.0} = \frac{2(F\ [kgf])\sin\left(\frac{136^\circ}{2}\right)}{d^2} = \frac{2(1\ [\text{kgf}])\sin\left(\frac{136^\circ}{2}\right)}{d^2} \qquad \text{Equation 2}$$

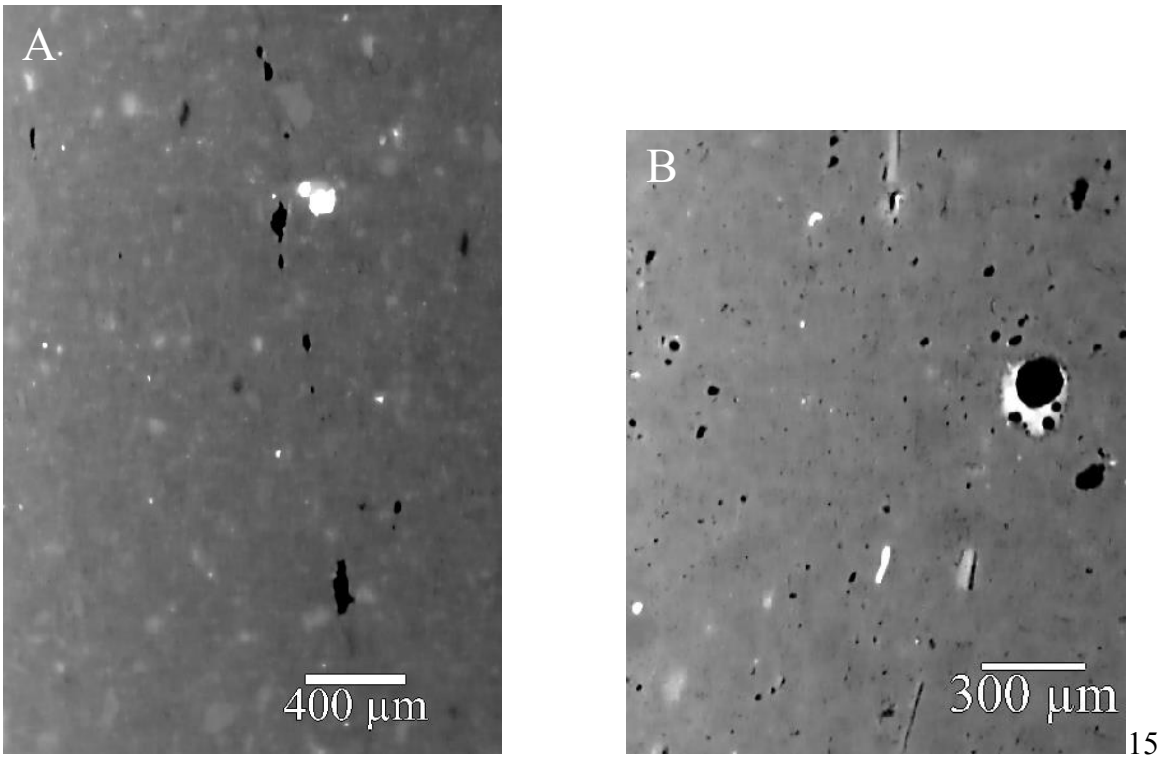

15

indentations were performed on each sample. The indentations were measured, and the hardness calculated from each indentation was recorded. These 15 hardness values for each sample were then averaged, culminating in a singular average hardness value representative of each fired sample.

Figure 9. Micro-CT image, of the unfired body, showing voids in black and more dense areas in grey to white. A) unfired sample (longitudinal cross section), B) fired, 998 ^{o}C (transverse cross section)

The sample fired to 998 ºC, following the procedure described above, had an average hardness of 70.76 HV1.0. The sample fired to 1152 ºC had an average hardness of 481.74 HV1.0. Thus, a more than six-fold increase in hardness was observed between the 998 ºC and 1152 ºC fired samples. This increase in hardness is indicative of an increase in overall strength, which were also observed in the three-point bend testing results given earlier. The growth of the mullite phase may be responsible for this increase in hardness. [17] However, further testing would be necessary to definitively evaluate the role mullite plays in improved observed mechanical properties.

Conclusions

Belle Fourche Shale (BFA) was processed (sub 150 μm size fraction) and characterized for use as a clay-based ceramic. The median particle size was approximately 10 μm and SEM images showed primarily layered clay particles. Wet BFS samples were rolled into a green body, dried at room temperature, fired (998 ºC, orange in color), and contained roughly 6 wt% hematite, 55% quartz, 19% microcline. When fired at 1152 ºC (red in color), mullite was found with increasing hematite compared to the 998 ºC fired sample. Micro-computed tomography (Micro-CT) of the unfired body exhibited very few large pores, the piece fired (998 ºC) also exhibited few and small pores, while the overall porosity of the fired body increased. Vickers Hardness values of 70.8 HV1.0 (998 ºC) and 485.7 HV1.0 (1152 ºC) were found for the fired pieces. Three-point bend testing gave an average strength of 23 MPa on pieces fired at 998 ºC and 55 MPa for the pieces fired at 1152 ºC. In summary, the research showed the efficacy of use of BFS for clay-based ceramic production.

Declarations: Funding and Competing/Conflicting Interests

This work was supported by the National Science Foundation Grant #2150356 REU Site: Back to the Future and Grant #2018626 MRI: Acquisition of a Focused Ion Beam Scanning

Electron Microscope for Research in Advanced Materials, Energy, and Environment. The authors have no relevant financial or non-financial interests to disclose.

The authors have no competing interests to declare that are relevant to the content of this article.

All authors certify that they have no affiliations with or involvement in any organization or entity with any financial interest or non-financial interest in the subject matter or materials discussed in this manuscript.

References

1. Hamer, F. and Hamer, J. (2015) *The Potter's Dictionary of Materials and Techniques. 6th edition,* Bloomsbury Academic.

2. Cadrin, A., Kyser, T., Caldwell, W., and Longstaffe, F. (1995) "Isotopic and chemical compositions of bentonites as paleoenvironmental indicators of the of the Cretaceous Western Interior Seaway," Paleaogeography, Palaeoclimatology, Palaeoecology. 119:301-32.

3. de Caritat, P., Bloch, J., Hutcheon, I., Longstaffe, F. (1994) "Compositional trends of a Cretaceous foreland basin shale (Belle Fourche Formation, Western Canada Sedimentary Basin): Diagenetic and Compositional Controls," Clay Minerals. 29:503-526.

4. Hutcheon, I., Longstaffe, F.J. and Abercrombie, H.J., "A comparison of shale compositions from the Western Canada Sedimentary Basin and the US Gulf Coast: the importance of depositional composition on shale diagcnesis," Mineralogical Magazine. 58A:150-151.

5. de Caritat, P., Bloch, J., Hutcheon, I., Longstaffe, F.J., Abercrombie, H.F., "Comparison of the mineralogical and chemical composition of two shales from the Western Canada Sedimentary Basin and the United States Gulf Coast," Clays Clay Miner. 45, 327–332 (1997). https://doi.org/10.1346/CCMN.1997.0450303

6. Schultz, L.G., Tourtelot, H.A., Gill, J.R., "Composition and properties of the Pierre Shale and equivalent rocks, northern Great Plains region." Professional Paper, 1064.1064-B (1980): 1-114.

7. United States Geological Survey, "Belle Fourche Shale", online link accessed 8/7/22, https://mrdata.usgs.gov/geology/state/sgmc-unit.php?unit=SDKb%3B0

8. Deng, T. and Li, J. (2016), "Study on preparation of thermal storage ceramic by using clay shale," Ceramics International, 42:18128-18135.

9. Tang, X.L., Min, F.H, and Qi, W., "Preparation of pottery from shale," Key Engineering Materials, Vol. 336. Trans Tech Publications Ltd, 2007.

10. Hajjaji, M., and A. Khalfaoui. "Oil shale amended raw clay: Firing transformations and ceramic properties," Construction and Building Materials, 23.2 (2009): 959-966.

11. Ouahabi, M. E., Daoudi, L., Hatert, F., and Fagel, N., "Modified mineral phases during clay ceramic firing," Clays and Clay Minerals, 63.5 (2015): 404-413.

12. Lao, X., Xu, X., Jiang, W., Liang, J., Miao, L., and Wu, Q. (2020), "Influences of impurities and mineralogical structure of different kaolin minerals on thermal properties of cordierite ceramics for high-temperature thermal storage," Applied Clay Science, *187*, 105485.

13. Nakamura, Y., Sakai, Y., Azuma, M., and Ohkoshi, S. I. (2020). "Long-term heat-storage ceramics absorbing thermal energy from hot water," Science Advances, *6*(27), eaaz5264

14. Cuffari, B., AZO Materials, "Using ceramics in energy storage," October 2016, online link accessed 8/7/22, https://www.azom.com/article.aspx?ArticleID=13230

15. Fahrenbach, M.D., South Dakota Geological Survey, "Geologic Map of the Rapid City East Quadrangle, SD," 2018, online link accessed 11/11/22, https://www.sdgs.usd.edu/pubs/pdf/GQ24K-28_2018.pdf

16. ASTM International (2014) Standard Test Method for Flexural Strength of Advanced Ceramics at Ambient Temperature. Designation C1161-13.

17. Rodriguez-Navarro, C., Cultrone, G., Sanchez-Navas, A. and Sebastian, E., "TEM study of mullite growth after muscovite breakdown." American Mineralogist 88.5-6 (2003): 713-724.

18. Abraham, C., "A Beginner's Guide to (CIE) Colorimetry," online link accessed 8/27/23. https://medium.com/hipster-color-science/a-beginners-guide-to-colorimetry-401f1830b65a